

Synthesis of CO-tolerant Ni-Pt Rhombic Dodecahedra Bimetallic Electrocatalytic Nanoparticles

Gurvinder Singh,^{*[a, b]} Svein Sunde,^[a] and Frode Seland^[a]

Abstract: Developing scalable synthetic routes for fabricating low-cost CO-tolerant and highly active electrocatalysts have significant relevance for fuel cell applications. Here, we report a novel and rapid single step synthesis of Ni enriched bimetallic core-shell (Ni–Pt) rhombic dodecahedra nanoparticles (NPs) via the thermal decomposition of precursor in the presence of oleylamine. Electrochemical dealloying in acidic medium (0.1 M HClO₄) subjecting NPs to different potential cycles is employed to vary the chemical composition and morphologies of parent bimetallic core-shell NPs. As a result, rhombic dodecahedra NPs transform to different morphologies such as concave, nanocage (open structure), and squeezed nanocage. Our results reveal that concave

rhombic dodecahedra shaped electrocatalysts show high resistance to CO poisoning compare to core-shell, nanocage, and squeezed nanocage morphologies as well as commercial Pt/C electrocatalysts. The improved CO tolerant of concave rhombic dodecahedra bimetallic NPs results from the presence of optimal content of Ni along with Pt content at the surface. We also demonstrate that CO tolerance of concave bimetallic NPs can be changed by electrochemical parameters such as the scan rate and CO adsorption potential. Overall, the present study presents a conceptual strategy for achieving improved CO tolerance by change in the composition and morphologies of bimetallic core-shell NPs.

Introduction


Carbon supported Pt-based catalysts are the benchmark catalysts for the electrocatalytic reduction and oxidation taking place in fuel cells.^[1] For industrial applications, the majority of the hydrogen comes from fossil fuels by steam reforming or oxidation of methane/propane (~95%), and some remnants of carbon monoxide (CO) are inevitably present.^[2,3] CO also appears as an intermediate species during the electro-oxidation of small organic molecules such as methanol, formic acid, or ethanol.^[4–6] Pt-based electrocatalysts are very susceptible to poisoning by CO, even if the concentration of CO is below 10 ppm.^[7] CO can adsorb strongly on the Pt surface and deteriorates the fuel cell performance.^[8] Alloying Pt with non-noble metals is a promising approach to fabricate inexpensive and improved CO tolerant bimetallic electrocatalysts (PtM, where M=Fe, Ni, Co, Mo, Ru, Sn).^[9–16] The electronic effect (the position of d-band centre) and bifunctional or oxophilic effect (accelerating the removal of adsorbed CO by supplying species containing oxygen) are considered to play a vital role in improving the CO tolerance of bimetallic electrocatalysts.^[17–20]

It is known that the CO electro-oxidation reaction is highly structure sensitive.^[21,22] For example, Wang et al observed the multiple CO oxidation peaks (peak at very low potential, pre-peak and main peak) in the CO stripping voltammograms on Ru-modified Pt electrodes in alkaline solution.^[23] They also studied the origin of multiple peaks and proposed that the adsorption of OH species from the dissociation of water molecules is thermodynamically more favourable at low coordination sites (defects, steps, kinks) or more active sites Ru, hindering the diffusion of CO from the sites of high coordination number (*i.e.* terraces, less active sites). Therefore, CO oxidation occurs at different sites due to a much lower CO mobility in alkaline media, and multiple oxidation peaks thus appear in the CO stripping voltammogram. The multiplicity in the CO stripping peak also depends on CO adsorption potential.^[24] Two CO oxidation peaks (pre-peak and main peak) appear when the adsorption potential of CO is set to 0.2 V or below in CO stripping voltammograms of Pt single crystals in acidic solution. CO pre-oxidation peak disappears when CO adsorption potential is set to 0.35 V. The origin of the pre-peak seems most likely due to the stripping of weakly bonded CO to the surface or strongly bonded immobilized water molecules at certain adsorption sites that oxidize CO at the neighbouring sites.^[25]

It has been studied that surface segregation is an appropriate strategy to design CO tolerant electrocatalysts.^[14,26–30] Ni-segregated NiPt and Pt-segregated NiPt were obtained after the pre-treatment at 350 °C in H₂ and O₂ environments, respectively.^[14] The results showed improved CO tolerance of Ni-segregated NiPt compare to Pt-segregated and homogenous alloy NiPt NPs. Zhang *et al.* also reported a strategy to enhance CO tolerance by engineering the phase and surface composition of Pt₃Co bimetallic catalytic NPs.^[13] The surface composition

[a] Dr. G. Singh, Prof. S. Sunde, Prof. F. Seland
Department of Materials Science and Engineering
Norwegian University of Science and Engineering
Sem Selands vei, Trondheim 7491 (Norway)
E-mail: frode.seland@ntnu.no

[b] Dr. G. Singh
Current Address: School of Aerospace, Mechanical and Mechatronics
Engineering
The University of Sydney
Shepherd Street, Sydney, NSW 2008 (Australia)
E-mail: gurvinder.singh@sydney.edu.au

 Supporting information for this article is available on the WWW under <https://doi.org/10.1002/cnma.202000277>

of Pt₃Co NPs tuned via adsorbate-driven segregation at heat treatment under different conditions. CO tolerance of the treated NP catalysts decreased in the following order: Co-rich NPs (air, 300 °C) > intermetallic NPs (argon, 700 °C) > Pt-rich NPs (10% H₂/N₂, 700 °C). This variations in CO tolerance is caused by the electronic effect playing a role in weakening the CO adsorption and thus promoting CO oxidation to form intermediate species COOH_{ad}. The oxidation of intermediate species COOH_{ad} to CO₂ is facilitated by the bifunctional/oxophilic effect. Similarly, the tunability in the surface composition via adsorbate-driven segregation by heat treatment under different environments has also been investigated for the NiPt NP system.^[31–34] Therefore, alloying Pt with non-noble metal is emerged as a strategy to design CO tolerant electrocatalysts for fuel cells. However, how electrochemical dealloying of core-shell bimetallic nanoparticles (NPs) influence CO oxidation reaction in alkaline medium has not investigated in detail. Such understanding is imperative because the electrochemical dealloying can cause change in the surface structure, chemical composition and morphology of core-shell bimetallic NPs.

In this work, we report a one-step synthesis of core-shell (Ni–Pt) bimetallic NPs of rhombic dodecahedra shape via a thermal decomposition of precursor in the presence of oleylamine (OAm). OAm is widely used as a solvent, reducing agent and capping ligands in the synthesis of NPs.^[35] The synthesized bimetallic NPs were supported on carbon black. The chemical composition and morphology of core-shell NPs were changed by electrochemical dealloying (*i.e.* varying the number of potential cycles of core-shell NPs between 0.05 and 1.0 V in 0.1 M perchloric acid (HClO₄) solution). Electron microscopy and electrochemical techniques were used to investigate the

change in the composition and morphology of synthesized and electrochemical dealloyed Ni–Pt NPs. We also investigate CO oxidation reaction on various prepared NPs to measure CO poisoning resilience in alkaline medium. How experimental conditions such as scan rate and CO dosing potential influence CO oxidation reaction in alkaline medium were examined in this work.

Results and Discussion

The detailed synthesis procedure of Ni–Pt bimetallic NPs is described in the experimental section. Briefly, a typical synthesis involved the degassing of OAm solution containing Pt and Ni precursors at 120 °C for 30 min. The degassed solution slowly heated to 290 °C at the rate of 3 °C/min. After 30 min of reaction at 290 °C, the reaction mixture cooled down. NPs were dispersed in hexane after precipitating and cleaning with the mixture of toluene and isopropanol. Bright field (BF) scanning transmission electron microscopy (STEM) imaging of NPs reveals the rhombic dodecahedra morphology of bimetallic Ni–Pt NPs (Figure 1a). The size of NPs determined from BF STEM image was found to be 95 ± 8 nm. The rhombic dodecahedra morphology of NPs can be clearly seen in the scanning electron microscopy (SEM) image (Figure 1b). The rhombic dodecahedra shape is formed from twelve facets. High resolution (HR) TEM imaging of an individual NP shows the formation of single crystalline rhombic dodecahedral bimetallic NPs. The fast Fourier transform (FFT) corresponding to HRTEM image recorded along the [110] zone axis suggests that NPs are enclosed by the {110} crystallographic facets.

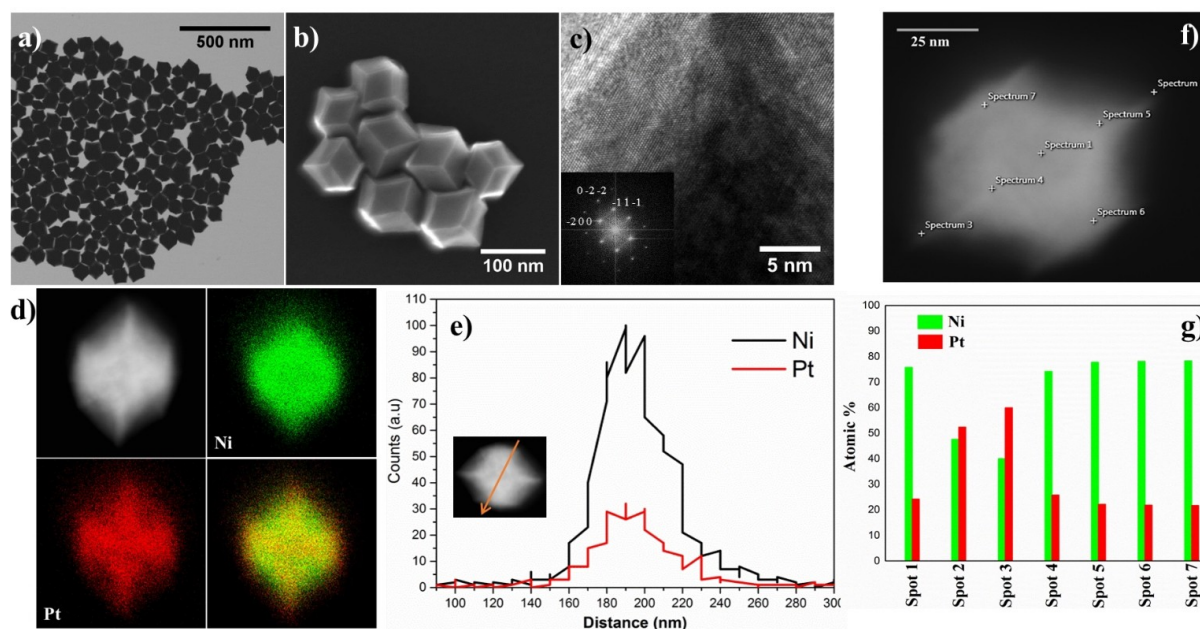


Figure 1. a) BF-STEM image of ~95 ± 8 nm Ni–Pt NPs, b) SEM image reveals rhombic dodecahedra morphology of NPs, c) HRTEM image of NPs (inset is the FFT). d) HAADF-STEM-EDS elemental mappings of single Ni–Pt NPs and e) HAADF-STEM-EDS line profile across a single NP. STEM-EDS analysis on different spots within a single Ni–Pt NPs shows the compositional inhomogeneity; f) HAADF-STEM image and g) atomic % of Ni and Pt measured from EDS spectra collected different spots.

In the chemical synthesis of noble metal NPs, organic ligands play a crucial role in tailoring the size, and morphology of NPs.^[36,37] In fcc (face centre cubic) metals, the surface energy of different crystallographic facets follows the trend; $\gamma\{110\} > \gamma\{100\} > \gamma\{111\}$.^[38] The growth of NP can be explained based on the interaction between organic ligands and various crystallographic facets as well as the relative growth rate of different facets. The concentration of monomers increases with the gradual increase in the temperature. When the concentration of monomers reaches supersaturation, the small nuclei form to lower the overall energy of the system. Initially, the concentration of monomers in the reaction mixture is high, the growth of NPs occurs uniformly. As the concentration of monomers drops down, the facet selective growth of NP takes place. OAm can be used as reducing agent and capping ligands, and these ligand molecules can bind preferentially to the facets of high surface energy to minimize its surface energy. In this case, the diffusion of monomers to the $\{110\}$ facets are hindered due to high packing density of ligand molecules on the $\{110\}$ facets. The monomers diffuse rapidly to the $\{100\}$ and $\{111\}$ facets because of the low packing density of OAm molecules on these surfaces. During the growth stage of the reaction, the growth of NPs occurs relatively faster on the $\{100\}$ and $\{111\}$ facets. Eventually, the $\{111\}$ and $\{100\}$ facets disappear, and Ni–Pt bimetallic NPs of rhombic dodecahedra shape enclosed by $\{110\}$ facets forms.

To determine the chemical composition and the structure of rhombic dodecahedra Ni–Pt bimetallic NPs, we used high-angle annular dark field (HAADF) STEM, energy dispersive spectroscopy (EDS), and X-ray diffraction (XRD) techniques. HAADF-STEM-EDS element mapping analysis suggests the distribution of Pt and Ni elements over a single NP (Figure 1d). Furthermore, the line profile shows a high content of Ni than to Pt in a single NP (Figure 1e). We also analyzed EDS spectra collected at various points across a single NP (Figure 1f and g). The results indicate a high Ni content at the centre of the NP (atomic ratio Pt to Ni: 1:3), and Ni content decreases with distance away from the centre. The average atomic ratio of Pt to Ni over a single NP was determined to be 1:3. Although, these results show the formation of Ni enriched Ni–Pt bimetallic NPs, the structure of NPs (*i.e.* alloy or core-shell) is not evident. To verify the structure of NPs, NPs were dispersed in 12 M acidic solution (hydrogen chloride (HCl)) for 24 hours. We did not observe any change in the morphology and the leaching of Ni from NPs even after 72 hours. An inductively coupled plasma optical emission spectrometer (ICP-OES) technique was also employed to determine the overall change in the ratio of Pt to Ni before and after the acid treatment. We did not observe a significant difference in the overall ratio of Pt to Ni before (1:2.9) and after (1:2.8) the acid treatment which is approximately closed to 1:3 ratio of Pt to Ni. Our results thus suggest the formation of acid stable core-shell rhombic dodecahedra NPs, *i.e.*, the surface of NP is enriched with Pt preventing the leaching of Ni from the core of NP into the solution, thus forming core-shell Ni–Pt NPs.

X-ray photoelectron spectroscopy (XPS) technique, which provides the elemental composition within 5–10 nm of the

surface, was used. XPS analysis indicates Pt enriched surface (Pt: 81.4 at% and Ni: 18.6 at%), verifying the evolution of core-shell bimetallic NPs (Figure S1). The surface composition of NPs before and after the acid treatment was also measured by XPS and the results show no significant difference in the surface composition of bimetallic NPs before and after the acid treatment (Figure S2). The formation of a core-shell structure can be understood based on the segregation energy of Pt and Ni atoms. The segregation energy of Pt atoms occupying at the edges (−1.99 eV) is more negative than atoms occupying at the surface (−1.73 eV) as well as the segregation energy of Ni that is positive (0.67 eV).^[39] This means, Pt has tendency to preferentially segregate to the edges than to the surface, and Ni preferentially segregates to the core. As a result, the edges of bimetallic NPs are enriched with Pt atoms followed by the enrichment of Pt atoms on the surface (few atomic layers), while the core of NPs is comprised of Ni atoms. These observations are consistent with EDS analysis suggesting the enrichment of Pt atoms at the edges and high concentration of Ni at the surface after a few Pt atomic layers. Furthermore, this also suggests that the difference in the reduction rate of Pt and Ni precursor leads to the design of core-shell NPs. The reduction rate of Pt precursor (Pt-OAm complex) is much faster than the reduction rate of Ni precursor (Ni-OAm complex) because OAm molecules (hard base) strongly coordinate with Ni²⁺ ions (hard acid), forming a strong metal-ligand complex.^[40,41] Initially, a high decomposition rate of Pt precursor leads to the supersaturated solution with Pt monomers and Pt nuclei form. As the reaction is progressed further, the concentration of Pt monomers falls due to the rapid depletion of Pt monomer in the nucleation stage, and Ni monomer concentration gradually increases in the solution. Ni monomers diffuse to the surface of Pt nanocluster and thus deposit on it. Since the segregation energy of Ni is more positive than Pt, Ni and Pt atoms migrate to the core and the surface of NPs, respectively. As a result, the core-shell bimetallic Ni–Pt NPs are evolved as a final product at the end of the synthesis. In the XRD data, the presence of (111), (200) and (220) reflections indicate the fcc crystal structure of the bimetallic NPs (Figure 2). The peaks in the diffractogram for the core-shell NPs lie between those of the two pure metals (*i.e.* they are shifted to higher diffraction angles with respect to pure Pt). Moreover, a shoulder peak to the right of the primary peak (111) can be noticed (inset of Figure 2). This shoulder peak position overlaps with pure Ni (111) peak, suggesting the presence of Ni-rich phase or Ni fcc phase in the NP. Taken together results from TEM, XPS, and XRD, these data support the formation of core-shell structure of rhombic dodecahedra Ni–Pt NPs.

We used the electrochemical leaching of carbon supported bimetallic NPs in an acidic environment. The chemical composition and morphology of NPs were altered and controlled by the number of potential cycles between 0.05 and 1.0 V with a scan rate of 500 mV/s in Ar-saturated 0.1 M HClO₄. Cyclic voltammogram (CV) of core-shell bimetallic NPs are displayed in Figure 3a. After 2 cycles, no difference can be seen in the morphology of NPs (NP-2). As the number of potential cycles increases from 2 to 30k (Figure 3a), CVs display to a larger extent the character-

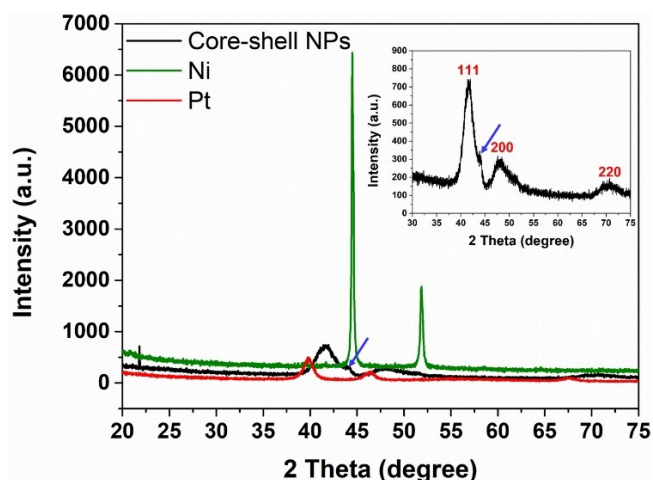


Figure 2. XRD patterns of rhombic dodecahedral shaped core-shell bimetallic (Ni-Pt) NPs, spherical Pt NPs, and spherical Ni NPs. Inset displays XRD pattern of core-shell NPs. Blue arrow indicates the shoulder peak.

istic feature of pure Pt in the underpotential hydrogen adsorption/desorption region (0.05–0.45 V). We also observed a broad Ni oxidation peak ($\text{Ni} \rightarrow \text{Ni}^{2+}$) in the positive scan (0.6 to 0.8 V) and a moderate Ni reduction peak ($\text{Ni}^{2+} \rightarrow \text{Ni}$) in the negative scan (0.7 to 0.4 V).^[42,43] The oxidation and reduction peaks of Ni disappear with the increase in the number of potential cycles, whereas a Pt hydroxide and Pt oxide peaks region in the range 0.7–1.0 V get stronger. After 30k potential cycles, the dealloyed sample does not exhibit any Ni features in the CV, implying that there are no residual Ni atoms in or in the vicinity of the surface. These results imply a change in the composition and morphology of electrochemically leached NPs with the increase in dealloying time (or increasing the number of potential cycles) in acidic medium. It is worth to point out that we did not observe any further change in the CV profile after exposing the NPs to more than 30k cycles.

Semi-quantitative information about the surface composition of the different electrocatalysts can be extracted by integrating the regions corresponding to the different surface species.^[44] The charge in the hydrogen adsorption/desorption (Q_H) region was calculated by integrating the CV between 0.05 to 0.45 V (Figure 3a), and the results are summarized in Table 1. The value of Q_H increases with the number of potential cycles, *i.e.*, $17 \mu\text{C cm}^{-2}$, $19 \mu\text{C cm}^{-2}$, $43 \mu\text{C cm}^{-2}$ and $46 \mu\text{C cm}^{-2}$ for NP-2, NP-200, NP-6k and NP-30k, respectively, thus pointing to a relative increase in Pt content at the surface with increasing dealloying time. The charge in Ni^{2+} ($Q_{\text{Ni}^{2+}}$) region was also determined to be $11 \mu\text{C cm}^{-2}$, $19 \mu\text{C cm}^{-2}$, and $3 \mu\text{C cm}^{-2}$ for NP-2, NP-200 and NP-6k, respectively (Table 1). A higher $Q_{\text{Ni}^{2+}}$ value for NP-200 than to NP-2 electrocatalysts can be noticed. This is due to the change in the surface composition of Pt and Ni contents caused by dissolution/redeposition of Pt atoms on the surface and exposure of Ni content from the core to the surface after the electrochemical cycling in the acidic medium. The surface charge of $Q_{\text{Ni}^{2+}}$ decreases after the increase in the electrochemical dealloying time (*i.e.* the increase in the number

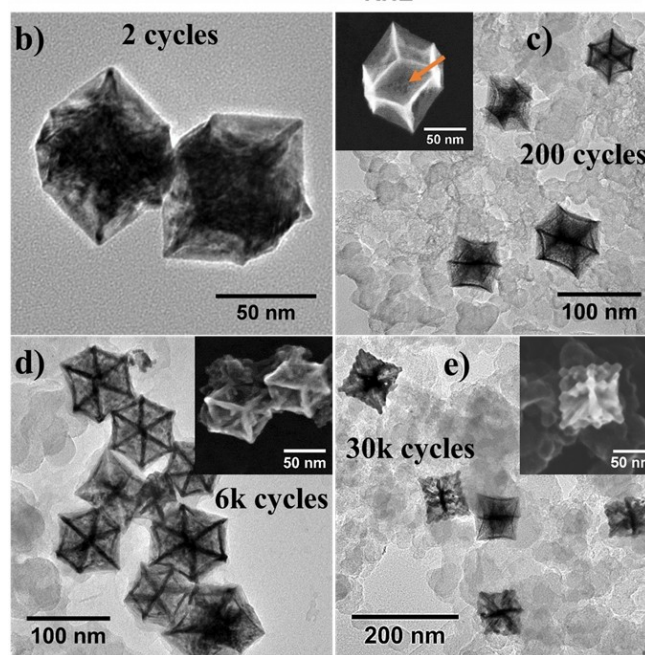
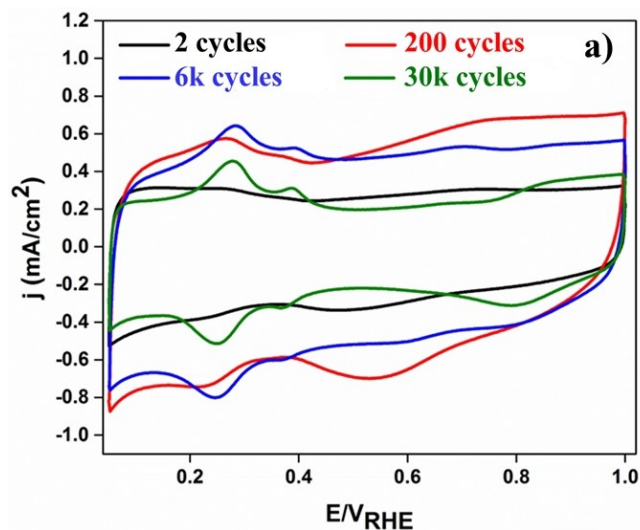


Figure 3. a) Cyclic voltammograms of Ni-Pt NPs after different potential sweeps in 0.1 M HClO_4 solution at the scan rate of 500 mV/s. TEM and inset SEM images show the NPs of different morphologies after different potential sweeps; b) core-shell rhombic dodecahedra NPs, c) concave rhombic dodecahedra NPs (arrow indicates the pits or holes in the NPs, *i.e.* the formation of porous NPs), d) nanocage morphology of NPs, and e) squeezed nanocage morphology of NPs.

of potential cycles from 200k to 6k and 30k) because of leaching of Ni contents from the NP in the acidic medium. To further evidence the surface composition of different NPs, we have collected and analyzed the XPS survey spectra. The results show the increase in Pt content and the decrease in Ni content on the surface of NPs as the number of potential cycles increases from 200k to 30k (Table S1). Therefore, the surface composition determined from XPS is nearly consistent with the surface composition measured by cyclic voltammogram.

TEM-EDS and SEM techniques used to examine the change in the morphology and chemical composition of dealloyed NPs

Table 1. Experimentally measured bulk (TEM-EDS), surface composition (CV) and charges measured from hydrogen adsorption (Q_H) and Ni^{2+} reduction ($Q_{Ni^{2+}}$) regions for different NPs. In NP-X, X refers to the number of potential cycles.

Sample	EDS measured composition of Pt:Ni (atomic ratio)	CV calculated surface composition	Q_H ($\mu C cm^{-2}$)	$Q_{Ni^{2+}}$ ($\mu C cm^{-2}$)
NP-2	0.47	Pt ₃ Ni	17	11
NP-200	1.24	Pt ₂ Ni	19	19
NP-6k	3.13	Pt ₂₈ Ni	43	3
NP-30k	6.47	Pt	46	

obtained after different number of potential sweeps in acidic medium. After 200 cycles, the morphology of bimetallic NPs (NP-200) changes from rhombic dodecahedra to concave rhombic dodecahedra (Figure 3c). The presence of small pits on the facets of NP-200 NPs implies the dissolution of Pt from the surface as well as Ni from the core (inset image in Figure 3c). It is likely that Pt atoms segregate to the edge and vertices of the NPs from the centre during the potential cycling because the segregation energies of atoms occupying at edges and vertices are lower than to atoms occupying at the centre.^[39] As the number of potential cycles increases to 6k, the complete removal of Ni from the core of NPs leads to the formation of the open structure of rhombic dodecahedra of NP (NP-6k), *i.e.*,

nanocage morphology similar to previously reported in the literature (Figure 3d).^[45,46] The edges and hollow interior of cycled NPs can clearly be seen in the inset SEM image of Figure 3d. After 30k cycles, the transformation of nanocage (open structure) into squeezed nanocage (NP-30k) with wavy or corrugated edges can be seen which is caused by the selective leaching of Ni content as well as Pt atomic dissolution/redeposition and rearrangement owing to electrochemical cycling (Figure 3e).^[47] TEM-EDS analysis performed on different type NPs reveals that the average atomic ratio of Pt to Ni increases as the number of potential cycles increases. This is due to the removal of Ni (equivalent to a relative increase in Pt content) during the electrochemical dealloying in acidic medium (Table 1). After 30k potential cycles, a complete dealloyed NPs do not show the presence of Ni content.

We studied the influence of morphologies and surface chemical compositions of core-shell and dealloyed electrocatalytic NPs on the oxidation reaction of preadsorbed CO. CO stripping voltammograms were collected in 0.1 M KOH and the potential sweep between 0.05 and 1.0 V with a scan rate of 50 mV/s. NP-2 and NP-200 electrocatalysts exhibit CO oxidation peak at low potential (~0.46 V) followed by a broader peak at a higher potential (~0.66 V) (Figures 4a and b). For NP-6k and NP-30k dealloyed electrocatalysts, the first peak can be seen at ~0.48 V, while the second peak at ~0.68 V becomes more pronounced and sharper with the appearance of a shoulder (Figure 4c and d). NP-2 and NP-200 electrocatalysts show the onset CO potential at ~0.35 V (the onset CO potential is defined

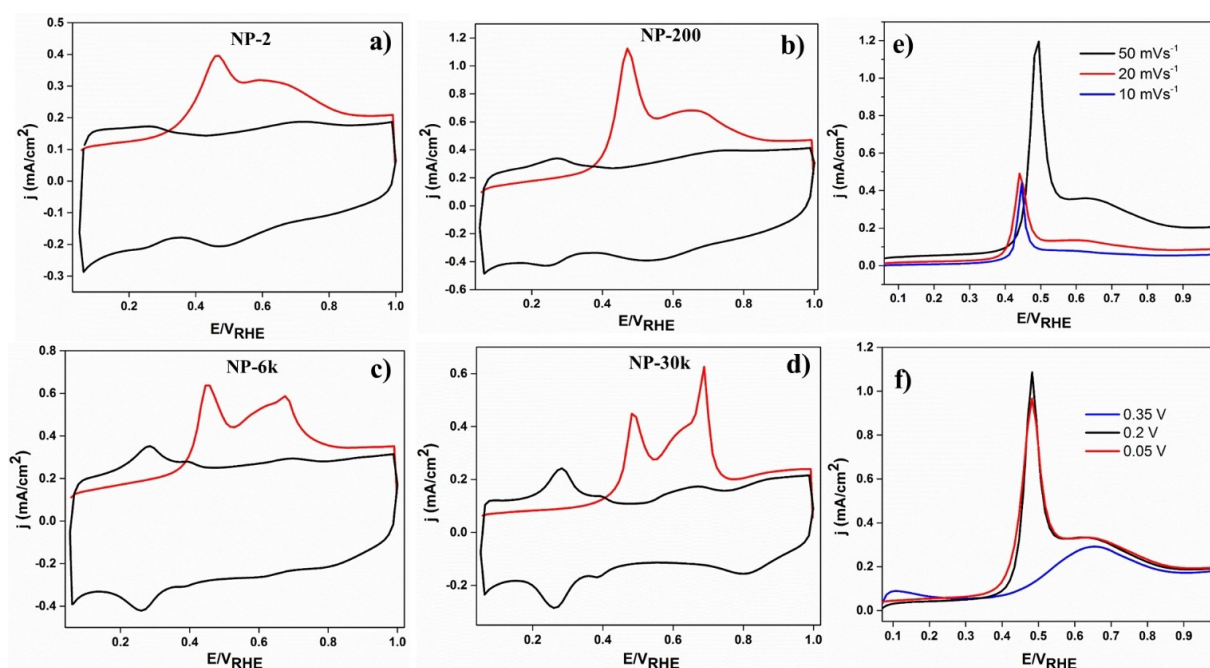


Figure 4. CO stripping voltammograms of different electrocatalysts in 0.1 M KOH solution with a scan rate of 50 mV/s. Red lines and black lines correspond to the CO stripping curve and background curve, respectively. The latter recorded as the following potential cycle in the absence of dissolved CO. The early CO oxidation charge (Q_{CO}^E) and total CO oxidation charge (Q_{CO}^T) were obtained from integrating the current responses in the potential regions between 0.3 to 0.52 V and 0.3 to 0.85 V, respectively. NPs of different compositions and morphologies were obtained after a) 2, b) 200, c) 6k and 30k of potential cycles in acidic medium. CO stripping voltammograms of NP-200 electrocatalysts at d) various scan rates (constant CO adsorption potential of 0.05 V) and f) different CO adsorption potentials (constant scan rate of 50 mV/s) in 0.1 M KOH solution.

as a potential at which when the slope of the voltammograms exceeded $0.005 \text{ mA cm}^{-2} \text{ mV}^{-1}$). This onset potential increases to $\sim 0.4 \text{ V}$ for Pt-riched electrocatalysts (NP-6k and NP-30k). Therefore, the characteristic difference in the oxidation reaction of CO among four different electrocatalysts of different surface compositions and morphologies can be observed.

We calculated CO oxidation charge of the linear background corrected first stripping cycle between 0.05 and 1.0 V.^[48,49] NP-200 electrocatalytic NPs show a maximum total CO stripping charge value of $Q_{\text{CO}}^{\text{T}} \sim 153 \mu\text{C cm}^{-2}$, while the other three samples NP-2, NP-6k and NP-30k exhibit lower CO stripping charges of 65, 96 and $64 \mu\text{C cm}^{-2}$, respectively. Instead of pursuing the overall charge, it is more interesting to note the charge difference between the first and second stripping peak with the extent of dealloying controlled by the number of potential cycles or time. The calculated charge ratio, $Q_{\text{CO}}^{\text{E}}/Q_{\text{CO}}^{\text{T}}$ (where Q_{CO}^{E} refers to Early CO oxidation charge, *i.e.*, charge corresponds to very low CO oxidation potential) are also given in Figure 4. NP-200 sample displays the highest ratio with approximately 61% of the overall CO stripping occurring in the lower potential peak region, significantly higher than the other samples, NP-2 (49%), NP-6k (40%) and NP-30k (35%). Electrocatalysts with reduced CO oxidation potential are desirable in order to avoid high anodic overpotentials. Based on the charge ratio for the various electrocatalysts, one can in a simplistic way rank electrocatalysts with respect to CO tolerance (or early CO stripping charge) in the order: NP-200 > NP-2 > NP-6k > NP-30k.

The difference in CO oxidation activity of distinct electrocatalysts can be linked to the variation in their surface composition. The electrochemical dealloying (selective removal of Ni atoms from parent NPs) in acidic media generates a favourable structural arrangement of Pt atoms at the surface of NPs (more active crystallographic facets or surfaces with beneficial Pt–Pt interatomic distances) for the oxidation of adsorbed CO molecules. The surface composition of NP-200 sample has low ratio of Pt to Ni, indicating the presence of Ni atoms on the surface. As a result, NP-200 electrocatalysts oxidize CO at low potential to a large extent in the presence of surface Ni oxides species (*i.e.* to a lesser extent Pt segregation on the surface). This is more likely from the bifunctional mechanism suggesting a reaction between Pt–CO_{ad} and Ni–OH_{ad}.^[20] The surface Ni sites act as an oxygen source for the CO oxidation and shift the CO stripping peak potential towards more negative potential. The Pt sites on the surface also contribute with oxygen to the CO stripping reaction through water activation or oxide formation, but only at the positive potentials (0.6–1.0 V). However, the impact of any electronic effect cannot be ruled out here.^[28,50] The addition of Ni make a significant contribution in modifying the electronic properties of Pt by supposedly decreasing the strength of Pt–CO bond due to a lowering of the Pt d-band in an alloy with Ni and thus shifting the peak potential of CO oxidation to more cathodic potential.^[51–53] Similarly, the presence of Ni also alters the bonding of water and the formation of oxides at the surface.

NP-2 electrocatalysts (core-shell NPs) show low CO tolerance than to NP-200 (concave rhombic dodecahedra NPs) due to the Pt enrichment on the surface (a low Ni content or QNi^{2+} value

for NP-2 than to NP-200). The presence of remained OAm traces on the surface of NP can also lead to low CO tolerance for NP-2, however, it is less likely the case due to the heat treatment of catalysts at 200°C for 3 hours and subsequently, electrochemical dealloying in acidic medium before the CO stripping experiment in the alkaline electrolyte. CO stripping charge related to the first oxidation peak decreases with the increase of surface Pt content (NP-6k and NP-30k samples behave like pure Pt surface). Therefore, the shift in the CO stripping peak potential and CO tolerance capability of electrocatalysts depend on the surface composition and morphologies of NPs, which can be changed by electrochemical dealloying subjected to the different potential cycles. The results suggest that the dealloying can be used as a suitable strategy to tune the electrocatalytic activity of NPs.

Furthermore, the multiple peaks in CO stripping profile of electrocatalysts can be seen. The origin of these multiple peaks is not known. However, these peaks may arise from the modification of the surface structures or morphologies of NPs (*i.e.* the formation of low coordination sites such as edges, vertices, defects and steps) by the different extent of electrochemical dealloying.^[23] These sites restrict the diffusion of CO molecules, and thus multiple peaks being observed in the CO stripping voltammograms. We compared CO oxidation reaction of electrocatalysts (parent and dealloyed NPs) produced in this work with commercial Pt/C electrocatalysts. The result of CO stripping and background voltammograms for a commercial Pt/C catalyst in 0.1 M KOH electrolyte are shown in Figure 5. A broad CO oxidation peak at a high positive potential ($\sim 0.72 \text{ V}$) is observed, preceded by two smaller shoulders at more negative potentials (0.4 and 0.6 V). The voltammetric features are clearly different those of NP-30k sample, supposedly only contain Pt in the surface, as well as other electrocatalytic samples (NP-2, NP-200 and NP-6k) showing distinct CO stripping features at more negative potentials compare to

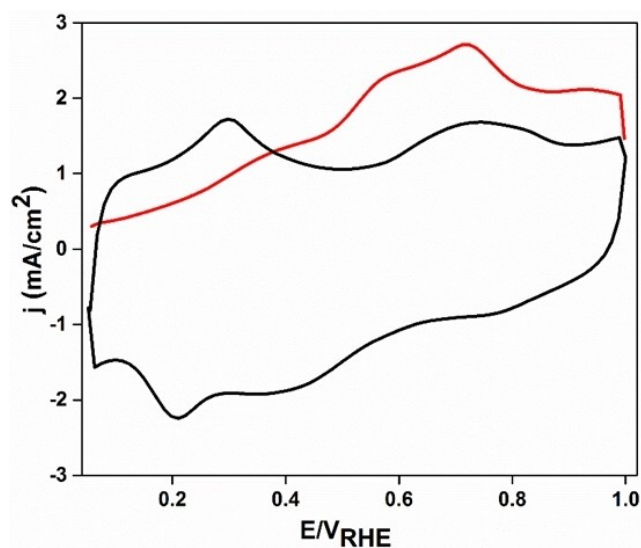


Figure 5. CO stripping voltammogram of commercial Pt/C (40% loading) in 0.1 M KOH solution at the scan rate of 50 mV/s.

commercial Pt/C electrocatalysts. It should be noted that we did not notice a significant difference in the CO tolerance of dealloyed NP-200 and other samples when these samples are electrochemically cycled in an alkaline solution prior to CO stripping experiment. This is due to the stability of dealloyed NPs in alkaline solution, thus preventing the migration of Ni contents to the solution or the change in the composition of NPs.

We choose NP-200 electrocatalysts to further investigate CO oxidation reaction at different scan rates and CO adsorption potential because NP-200 electrocatalysts show superior CO tolerance than to other electrocatalysts (NP-2, NP-6k and NP-30k). Figure 4e displays CO stripping voltammograms of NP-200 electrocatalysts at different scan rates. At low scan rate (10 mVs^{-1}), CO oxidation occurs at low potential (~ 0.44 V). However, CO oxidation peak shifts to higher potential (~ 0.49 V) at high scan rate (50 mVs^{-1}). These results imply that the oxidation of CO molecules from the different sites (edges, vertices, and steps) depends on the concentration of corresponding sites and time given to reach these sites.^[54] At a low scan rate, CO molecules can diffuse to active sites (to low coordination sites, including edges, vertices, steps or defects) and are oxidized there as sufficient time is given. In this case, all CO molecules oxidize at low potential. The diffusion of CO molecules is restricted at a high scan rate. In this case, CO molecules oxidize from different sites (*i.e.* from high coordination sites such as terraces). Therefore, the role of electronic effect (the binding strength of CO molecules with different sites on the surface) is crucial in controlling the CO oxidation reaction. Furthermore, a fast scan rate can lead to a decrease in the size of the diffusion layer, and a higher current was thus observed.^[55]

We also examined the effect of CO adsorption potential on the electrocatalytic activity of NP-200 (Figure 4f). In these experiments, CO was adsorbed to NP-200 electrocatalysts at different potentials, 0.05, 0.2 and 0.35 V. At CO adsorption potential ≤ 0.2 V, CO oxidation occurs at low potential (~ 0.46 V) followed by a broad weak peak at higher potential (~ 0.65 V). CO oxidation peak shifts to high potential (~ 0.65 V) when CO adsorption potential is increased to 0.35 V. We did not observe any shoulder or pre-oxidation peak in these cases. The adsorption of CO at 0.05, 0.2 and 0.35 V results in the Q_{CO}^T values of 149 $\mu\text{C cm}^{-2}$, 142 $\mu\text{C cm}^{-2}$ and 44 $\mu\text{C cm}^{-2}$, respectively. This implies that CO coverage decreases significantly with the increase in CO adsorption potential to 0.35 V. It is most likely due to the partial oxidation of CO molecules during CO adsorption at higher adsorption potentials.^[56–58] However, most of CO molecules diffused to the site of low energy and remained unoxidized in the adsorbed layer. The oxidation of these remaining CO molecules requires the generation of oxygen donating species at these sites, for instance, some form of surface bonded water, which occurs only at more positive potential.

Conclusion

In summary, we demonstrated the synthesis of bimetallic core-shell (Ni–Pt) NPs of rhombic dodecahedra morphology via the decomposition of precursors at high temperature. The approach does not require two-step synthesis strategy involving the deposition of shell on the preformed seed particles. The strong binding of OAm capping ligands to the {110} crystallographic facets facilitates the formation of rhombic dodecahedra shape of NPs. TEM-EDS, SEM, XRD and XPS results reveal the formation of bimetallic core-shell (Ni–Pt) NPs of rhombic dodecahedra shape. The morphology and chemical composition of bimetallic core-shell NPs can be altered by electrochemical dealloying in the acidic medium at different potential cycles (or dealloying time). As a result, bimetallic core-shell NPs transform into various morphologies, including concave rhombic dodecahedra (NP-200), nanocage (NP-6k) and squeezed nanocages (NP-30k). CO stripping voltammetry measurements in alkaline medium showed that CO tolerance of different electrocatalysts follows the trend; NP-200 (concave rhombic dodecahedra NPs) > NP-2 (core-shell rhombic dodecahedra NPs) > NP-6k (open structure or nanocage of rhombic dodecahedra) > NP-30k (squeezed nanocage of rhombic dodecahedra). The difference in the surface structure, composition and morphology of electrocatalysts causes the difference in oxophilic and electronic effects, which play an important role in improving the CO tolerance of Ni–Pt based electrocatalysts. Our results also demonstrate the dependence of the CO tolerance of electrocatalytic NPs on the experimental parameters such as the scan rate and CO adsorption/dosing potential. The present study thus advances our understanding to design CO-tolerant bimetallic electrocatalysts, and highlights the importance of the surface structure, composition and morphology in improving the CO tolerance of NPs. The finding of our study will provide new rules for designing novel bimetallic electrocatalysts for methanol oxidation, oxygen reduction and hydrogen evolution reactions for the alkaline system.

Experimental Section

Chemicals. Chloroplatinic acid hexahydrate ($\text{H}_2\text{PtCl}_6 \cdot 6\text{H}_2\text{O}$, > 99.9%), nickel (II) nitrate hexahydrate ($\text{Ni}(\text{NO}_3)_2 \cdot 6\text{H}_2\text{O}$, 99.9%), Oleylamine (70%, technical grade), potassium hydroxide (0.1 M KOH) and Nafion (5%) were purchased from Sigma-Aldrich, and used without further purification. Carbon black (Vulcan XC-72, Cabot) was purchased from Cabot. Perchloric acid (70%, HClO_4) was received from Merck AS.

Synthesis. For the synthesis of rhombic decahedral Pt–Ni NPs, $\text{H}_2\text{PtCl}_6 \cdot 6\text{H}_2\text{O}$ (40 μmol) and $\text{Ni}(\text{NO}_3)_2 \cdot 6\text{H}_2\text{O}$ (74 μmol) were added to 12 mL oleylamine and sonicated for 30 min to ensure the solubilization of both precursors. Oleylamine shows a high binding affinity to metal ions through its amine ($-\text{NH}_2$) group. Therefore, Pt and Ni salts form complexes with oleylamine. The reaction mixture was transferred to 100 mL double necked round bottom flask and heated to 120 °C at a heating rate of 10 °C/min. After degassing for 30 min, the reaction mixture was heated slowly to 290 °C at a heating rate of 3 °C/min under an argon (Ar) atmosphere. The reaction mixture was kept at 290 °C for 30 minutes. After the

reaction, the solution was cooled down to room temperature. NPs were precipitated by adding 5 mL toluene and 20 mL isopropanol and centrifuged at 5000 rpm for 5 min. The NPs were washed twice with toluene and isopropanol, and finally, dispersed in toluene.

Characterization techniques. Bright field (BF) and dark field (DF) scanning transmission electron microscopy (STEM) and scanning electron microscopy (SEM) images were collected from Hitachi S-5500 operating at 30 kV. High-resolution (HR) transmission electron microscopy (TEM) imaging, energy dispersive spectroscopy (EDS) and high-angle annular dark field (HAADF)-STEM analysis were performed with field emission JEOL 2100F TEM operating at 200 kV. A Bruker DaVinci2 diffractometer with Cu K α radiation ($\lambda = 1.5418 \text{ \AA}$) was used to collect X-ray diffraction (XRD) pattern of NPs. For XRD, the NP solution was deposited on a single crystalline silicon holder and dried. The X-ray photoelectron spectroscopy (XPS) data were obtained using a Kratos Axis Ultra DLD spectrometer (Kratos Analytical), equipped with a monochromatized aluminium X-ray source (AlK, $h\nu = 1486.6 \text{ eV}$) operating at 15 mA and 15 kV (225 kW). The XPS data were analyzed with CASA XPS software. Inductively coupled plasma optical emission spectrometer (ICP-OES; Optima 5300DV) was used to determine the accurate Pt and Ni contents in the bimetallic NPs before and after the acid treatment.

Electrode preparation. NPs were supported on carbon black (Vulcan XC-72, Cabot) as follows: 10 mg catalytic NPs and 40 mg carbon black were dispersed separately in 10 mL hexane by sonication. Later, both solutions were mixed and sonicated for 1 h at 60 °C in a closed glass vial. The supported catalyst was washed three times with ethanol by centrifugation at 5000 rpm and dried in air at room temperature. Later, the product was heat treated at 200 °C in vacuum for 3 h to remove organic surfactants. The catalytic ink (2 mg/mL) was prepared in the water and isopropanol mixture (4:1), and 20 μL of a diluted Nafion (0.5% v/v) was added to the ink. Two drops of 10 μL catalyst ink was transferred to a glassy carbon electrode (5 mm in diameter, Pine instrument), and dried in vacuum.

Electrochemical measurements. An Autolab potentiostat, (PGSTAT302N) was used to perform electrochemical measurements in a conventional three-electrode electrochemical cell with a reversible hydrogen reference electrode. Prior to the electrochemical measurements, the electrolyte (0.1 M KOH, purchased from Sigma-Aldrich) was degassed by purging Ar through it for 30 min. Cyclic voltammograms (CVs) were obtained by sweeping the potential from 0.05 to 1 V at a scan rate of 100 mV/s at room temperature. For the CO-stripping experiments, first CO gas bubbled through the electrolyte solution for 10 min at 0.05 V. Ar was subsequently flushed through the solution for 30 min to remove dissolved CO. CO stripping voltammograms were recorded at a scan rate of 50 mV/s between 0.05 and 1 V. The electrochemical dealloying of the catalytic NPs was performed in the potential range 0.05–1.0 V at a scan rate of 500 mV/s in 0.1 M HClO $_4$ solution. All potentials in this work are referenced to the reversible hydrogen electrode (RHE). The current density (J) and surface charge (Q) are normalized in reference to the geometric area of glassy carbon electrode (0.196 cm 2) in all cyclic and CO stripping voltammograms.

Acknowledgements

The Research Council Norway (Project no. 221899) acknowledge for supporting the work. The Research Council of Norway is also acknowledged for the support to the Norwegian Micro- and Nano-Fabrication Facility, NORFAB (245963).

Conflict of Interest

The authors declare no conflict of interest.

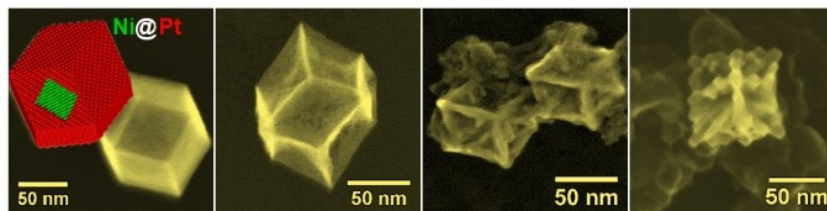
Keywords: Bimetallic electrocatalysts · nanocage · dealloying · CO tolerant · nanoparticles

- [1] X. Ren, Q. Lv, L. Liu, B. Liu, Y. Wang, A. Liu, G. Wu, *Sustainable Energy Fuels* **2020**, *4*, 15–30.
- [2] G. Voitic, S. Nestl, K. Malli, J. Wagner, B. Bitschnau, F.-A. Mautner, V. Hacker, *RSC Adv.* **2016**, *6*, 53533–53541.
- [3] N. Armaroli, V. Balzani, *ChemSusChem* **2011**, *4*, 21–36.
- [4] A. B. Anderson, H. A. Asiri, *Phys. Chem. Chem. Phys.* **2014**, *16*, 10587–10599.
- [5] J. Bai, D. Liu, J. Yang, Y. Chen, *ChemSusChem* **2019**, *12*, 2117–2132.
- [6] T. Iwasita, *Electrochim. Acta* **2002**, *47*, 3663–3674.
- [7] H. Igarashi, T. Fujino, M. Watanabe, *J. Electroanal. Chem.* **1995**, *391*, 119–123.
- [8] W.-M. Yan, H.-S. Chu, M.-X. Lu, F.-B. Weng, G.-B. Jung, C.-Y. Lee, *J. Power Sources* **2009**, *188*, 141–147.
- [9] Z. Liu, G. S. Jackson, B. W. Eichhorn, *Angew. Chem. Int. Ed.* **2010**, *49*, 3173–3176.
- [10] J. Svendby, F. Seland, G. Singh, J. L. G. de la Fuente, S. Sunde, *J. Electroanal. Chem.* **2019**, *833*, 189–197.
- [11] T. Sato, K. Kunimatsu, K. Okaya, H. Yano, M. Watanabe, H. Uchida, *Energy Environ. Sci.* **2011**, *4*, 433–438.
- [12] Z. Liu, J. E. Hu, Q. Wang, K. Gaskell, A. I. Frenkel, G. S. Jackson, B. Eichhorn, *J. Am. Chem. Soc.* **2009**, *131*, 6924–6925.
- [13] B.-W. Zhang, Z.-C. Zhang, H.-G. Liao, Y. Gong, L. Gu, X.-M. Qu, L.-X. You, S. Liu, L. Huang, X.-C. Tian, R. Huang, F.-C. Zhu, T. Liu, Y.-X. Jiang, Z.-Y. Zhou, S.-G. Sun, *Nano Energy* **2016**, *19*, 198–209.
- [14] M. Ahmadi, F. Behafarid, C. Cui, P. Strasser, B. R. Cuenya, *ACS Nano* **2013**, *7*, 9195–9204.
- [15] G. Shi, H. Yano, D. A. Tryk, A. Iiyama, H. Uchida, *ACS Catalysis* **2017**, *7*, 267–274.
- [16] J. Li, Z. Luo, F. He, Y. Zuo, C. Zhang, J. Liu, X. Yu, R. Du, T. Zhang, M. F. Infante-Carrió, P. Tang, J. Arbiol, J. Llorca, A. Cabot, *J. Mater. Chem. A* **2018**, *6*, 22915–22924.
- [17] V. R. Stamenkovic, B. S. Mun, K. J. J. Mayrhofer, P. N. Ross, N. M. Markovic, *J. Am. Chem. Soc.* **2006**, *128*, 8813–8819.
- [18] Y. Wang, G. Wang, G. Li, B. Huang, J. Pan, Q. Liu, J. Han, L. Xiao, J. Lu, L. Zhuang, *Energy Environ. Sci.* **2015**, *8*, 177–181.
- [19] K.-W. Park, J.-H. Choi, B.-K. Kwon, S.-A. Lee, Y.-E. Sung, H.-Y. Ha, S.-A. Hong, H. Kim, A. Wieckowski, *J. Phys. Chem. B* **2002**, *106*, 1869–1877.
- [20] C. Roth, N. Benker, R. Theissmann, R. J. Nichols, D. J. Schiffrin, *Langmuir* **2008**, *24*, 2191–2199.
- [21] M. T. Koper, *Nanoscale* **2011**, *3*, 2054–2073.
- [22] P. Rodríguez, G. García, E. Herrero, J. M. Feliu, M. T. M. Koper, *Electrocatalysis* **2011**, *2*, 242–253.
- [23] H. Wang, H. D. Abruña, *J. Phys. Chem. Lett.* **2015**, *6*, 1899–1906.
- [24] M. J. S. Farias, C. Busó-Rogero, F. J. Vidal-Iglesias, J. Solla-Gullón, G. A. Camara, J. M. Feliu, *Langmuir* **2017**, *33*, 865–871.
- [25] J. S. Spendelow, J. D. Goodpaster, P. J. A. Kenis, A. Wieckowski, *J. Phys. Chem. B* **2006**, *110*, 9545–9555.
- [26] T. Li, R. Wang, M. Yang, S. Zhao, Z. Li, J. Miao, Z.-D. Gao, Y. Gao, Y.-Y. Song, *Sustainable Energy Fuels* **2020**, *4*, 380–386.
- [27] L. Peng, E. Ringe, R. P. Van Duyne, L. D. Marks, *Phys. Chem. Chem. Phys.* **2015**, *17*, 27940–27951.
- [28] V. R. Stamenkovic, B. S. Mun, M. Arenz, K. J. Mayrhofer, C. A. Lucas, G. Wang, P. N. Ross, N. M. Markovic, *Nat. Mater.* **2007**, *6*, 241–247.
- [29] H. Liao, A. Fisher, Z. J. Xu, *Small* **2015**, *11*, 3221–3246.
- [30] S. Zafeirotas, S. Piccinin, D. Teschner, *Catal. Sci. Technol.* **2012**, *2*, 1787–1801.
- [31] Y.-T. Pan, H. Yang, *Nano Today* **2020**, *31*, 100832–100845.
- [32] L. Gan, M. Heggen, C. Cui, P. Strasser, *ACS Catalysis* **2016**, *6*, 692–695.
- [33] M. Gocyla, S. Kuehl, M. Shviro, H. Heyen, S. Selve, R. E. Dunin-Borkowski, M. Heggen, P. Strasser, *ACS Nano* **2018**, *12*, 5306–5311.
- [34] Y.-T. Pan, J. Wu, X. Yin, H. Yang, *E. AICCh, Journal* **2016**, *62*, 399–407.
- [35] S. Mourdikoudis, L. M. Liz-Marzán, *Chem. Mater.* **2013**, *25*, 1465–1476.
- [36] X. Yin, M. Shi, J. Wu, Y. T. Pan, D. L. Gray, J. A. Bertke, H. Yang, *Nano Lett.* **2017**, *17*, 6146–6150.

- [37] X. Yin, X. Liu, Y. T. Pan, K. A. Walsh, H. Yang, *Nano Lett.* **2014**, *14*, 7188–7194.
- [38] Y. Xia, X. Xia, H. C. Peng, *J. Am. Chem. Soc.* **2015**, *137*, 7947–7966.
- [39] L. Wang, Y. Yang, N. Wang, S. Huang, *Comput. Mater. Sci.* **2016**, *117*, 15–23.
- [40] A. Vivien, M. Guillaumont, L. Meziane, C. Salzemann, C. Aubert, S. Halbert, H. Gérard, M. Petit, C. Petit, *Chem. Mater.* **2019**, *31*, 960–968.
- [41] J. L. Reyes-Rodríguez, A. Velázquez-Osorio, D. Bahena-Urbe, A. B. Soto-Guzmán, M. A. Leyva, A. Rodríguez-Castellanos, S. Citalán-Cigarroa, O. Solorza-Feria, *Catal. Sci. Technol.* **2019**, *9*, 2630–2650.
- [42] R. M. A. Tehrani, S. Ab Ghani, *Fuel Cells* **2009**, *9*, 579–581.
- [43] C. Zhang, *J. Electrochem. Soc.* **1987**, *134*, 2966–2970.
- [44] J. Suntivich, Z. Xu, C. E. Carlton, J. Kim, B. Han, S. W. Lee, N. Bonnet, N. Marzari, L. F. Allard, H. A. Gasteiger, K. Hamad-Schifferli, Y. Shao-Horn, *J. Am. Chem. Soc.* **2013**, *135*, 7985–7991.
- [45] C. Chen, Y. Kang, Z. Huo, Z. Zhu, W. Huang, H. L. Xin, J. D. Snyder, D. Li, J. A. Herron, M. Mavrikakis, M. Chi, K. L. More, Y. Li, N. M. Markovic, G. A. Somorjai, P. Yang, V. R. Stamenkovic, *Science* **2014**, *343*, 1339–1343.
- [46] N. Becknell, Y. Kang, C. Chen, J. Resasco, N. Kornienko, J. Guo, N. M. Markovic, G. A. Somorjai, V. R. Stamenkovic, P. Yang, *J. Am. Chem. Soc.* **2015**, *137*, 15817–15824.
- [47] D. M. Kolb, *Prog. Surf. Sci.* **1996**, *51*, 109–173.
- [48] T. Vidaković, M. Christov, K. Sundmacher, *Electrochim. Acta* **2007**, *52*, 5606–5613.
- [49] S. Rudi, C. Cui, L. Gan, P. Strasser, *Electrocatalysis* **2014**, *5*, 408–418.
- [50] F. Bortoloti, A. C. Garcia, A. C. D. Angelo, *Int. J. Hydrogen Energy* **2015**, *40*, 10816–10824.
- [51] M. T. M. Koper, T. E. Shubina, R. A. van Santen, *J. Phys. Chem. B* **2002**, *106*, 686–692.
- [52] M. Tsuda, H. Kasai, *Phys. Rev. B* **2006**, *73*, 155405–1554013.
- [53] A. Ruban, B. Hammer, P. Stoltze, H. L. Skriver, J. K. Nørskov, *J. Mol. Catal. A: Chem.* **1997**, *115*, 421–429.
- [54] G. García, M. T. M. Koper, *Phys. Chem. Chem. Phys.* **2008**, *10*, 3802–3811.
- [55] N. Elgrishi, K. J. Rountree, B. D. McCarthy, E. S. Rountree, T. T. Eisenhart, J. L. Dempsey, *J. Chem. Educ.* **2018**, *95*, 197–206.
- [56] T. Kawaguchi, W. Sugimoto, Y. Takasu, *Electrochemistry* **2010**, *78*, 36–41.
- [57] A. López-Cudero, Á. Cuesta, C. Gutiérrez, *J. Electroanal. Chem.* **2006**, *586*, 204–216.
- [58] S. T. Briskeby, M. Tsytkin, R. Tunold, S. Sunde, *RSC Adv.* **2014**, *4*, 44185–44192.

Manuscript received: April 28, 2020
 Revised manuscript received: May 28, 2020
 Accepted manuscript online: May 28, 2020
 Version of record online: ■■■, ■■■■

FULL PAPER



Electrochemical dealloying time

An approach based on thermal decomposition is used to synthesize bimetallic core-shell (Ni@Pt) nanoparticles of rhombic dodecahedra shape. The morphology and chemical composition can be changed by electro-

chemical dealloying time of core-shell nanoparticles. The work thus opens up new ways to tailor the composition and morphology of nanoparticles, thus enabling the development of CO-tolerant bimetallic electrocatalysts.

Dr. G. Singh, Prof. S. Sunde, Prof. F. Seland*

1 – 10

Synthesis of CO-tolerant Ni-Pt
Rhombic Dodecahedra Bimetallic
Electrocatalytic Nanoparticles

